

Revealing shape variability and cultivar effects on cooling of packaged fruit by combining CT-imaging with explicit CFD modelling

W. Gruyters^(a), T. Van De Looverbosch^(a), Z. Wang^(a), S. Janssen^(a), P. Verboven^(a), T. Defraeye^(b), B. M. Nicolai^(a, c *)

^a BIOSYST-MeBioS, Katholieke Universiteit Leuven, Willem de Croylaan 42, B-3001 Leuven, Belgium

^b Empa, Swiss Federal Laboratories for Materials Science and Technology, Laboratory for Biomimetic Membranes and Textiles, Lerchenfeldstrasse 5, 9014 St. Gallen, Switzerland

^c Flanders Centre of Postharvest Technology, Willem de Croylaan 42, B-3001 Leuven, Belgium

*Corresponding author;

email: bart.nicolai@kuleuven.be – telephone number: +32 16 32 23 75

Abstract

Proper postharvest temperature management is required to maintain the quality of fresh fruit such as pears. Understanding and evaluating the cooling process is crucial. In this context, numerical modelling techniques such as computational fluid dynamics (CFD) can provide complementary insights to experimental measurements. Fruit come in a variety of shapes that are also cultivar-dependent. In this work, CFD modelling was combined with X-ray computed tomography (CT) to explore the differences in cooling characteristics of different pear fruit cultivars in cardboard boxes, as determined by variable fruit shape. First, CT images of boxes randomly filled with pear fruit were obtained. Next, horizontal forced-air cooling experiments with three different pear cultivars (cv. ‘Doyenné’, cv. ‘Conference’ and cv. ‘Durondeau’) were conducted in a pre-cooling setup. After CT image reconstruction of the box and fruit CAD geometry, CFD simulations with the actual pear filling were developed and validated with experimentally-obtained cooling profiles. The experimental data agreed very well with simulation results of three cultivars. Shape differences led to internal porosity variation of the fruit filled box that determined local airflow patterns and cooling behaviour. The cooling time of individual pears in a box differed up to 4 h and large

32 differences in cooling time between the boxes with different pear cultivars were observed.
33 Individual fruit shapes clearly influence cooling behaviour. This work demonstrates that
34 cooling results depend on the filling pattern, so that several fillings need to be accounted for
35 to have a realistic statistical average, which can be achieved by a previously developed shape
36 model combined with discrete element modelling and CFD.

37 **Keywords:** computational fluid dynamics; pear; forced-air cooling; biological variability;
38 X-ray computed tomography; porosity
39

40 **Highlights**

- 41 • CFD was solved on geometry obtained from X-ray computed tomography (CT)
- 42 • Fruit shape led to complex internal porosity variation of fruit filled boxes
- 43 • Different pear cultivars resulted in different filling structure properties
- 44 • Local airflow patterns and fruit cooling rates in the box were affected by pear shape

45

1 Introduction

From the moment that fresh pome fruit are harvested, they solely rely on their internal energy reserves, accumulated during growth, as a fuel for their respiration metabolism (Jackson, 2003; Kader, 2002). By minimising their postharvest respiration process, the speed of senescence and deterioration is slowed down and fruit quality is maintained for a longer period (Prusky, 2011). This is often achieved right after harvest by rapidly cooling the produce to lower temperatures with forced-air cooling (FAC) (Brosnan and Sun, 2001; Taiz et al., 2015). Evaluating and improving the postharvest cooling processes is crucial for product quality, uniformity, energy efficiency and throughput. In FAC cool air is blown over the products that are usually filled inside dedicated packaging for ease of transport. Packaging provides a significant barrier for the air to reach and cool the fruit, while the fruit stack affects uniformity of the cooling rate (Gruyters et al., 2018). Towards this end, numerical modelling techniques such as computational fluid dynamics (CFD) can provide complementary insights for improved packaging design towards more energy-efficient and uniform cooling (Berry et al., 2017; Wu et al., 2018; Zhao et al., 2016).

In CFD modelling, the complex features of the solid geometries (produce and package material) can be explicitly taken into account, by modelling these objects discretely. In previous research, the fruit stacks were often approximated with simplified regular geometries such as spheres (Ambaw et al., 2017; Defraeye et al., 2013a; Delele et al., 2013a). For spherically-shaped produce such as oranges or apples, the average cooling process can be predicted fairly well (Defraeye et al., 2014; Han et al., 2017; Lu et al., 2016). The cooling behaviour of non-spherical fruit such as pears is, however, more complex: because of their shape, their filling pattern is much different from that of spherical fruit and likely affects the local air flow and heat transfer considerably. To have a realistic cooling behaviour prediction with CFD, it is advised that their actual fruit shape is incorporated in the CFD model.

In a first attempt to recreate a realistic fruit filling pattern in packaging, Ferrua and Singh made use of a single realistic strawberry fruit shape in a numerical FAC study (Ferrua and Singh, 2009a, 2009b, 2009c). This single fruit shape was used to manually create a geometric model of the filling pattern of a series of identical strawberries in a clamshell. Both generating the single fruit shape and the entire filling pattern were, however, very time consuming. With the validated geometrical model generator, developed by Rogge et al. (Rogge et al., 2015, 2014), it has become possible to quickly generate numerous realistic 3D shape models, and incorporating biological variability of size and shape, implying a statistical variation on the average fruit shape. By coupling this model generator with a discrete element software (Diels et al., 2016; Smeets et al., 2014) it was possible to generate realistic filling patterns for CFD simulations, as was demonstrated by Gruyters et al. (2018). However, these filling patterns were generated in-silico so entirely virtual, as no real-life equivalent was available for experimental validation. As such, validation of CFD simulations incorporating these patterns is only possible in a statistical way by comparing simulations of a series of randomly generated patterns with experimental measurements in a series of actual stacked boxes. There is thus a need for a more direct validation method for a CFD model of a fruit stack, and this requires an accurate geometrical model of the actual fruit filled in a cardboard box, which is used for the validation measurements.

Reconstructing a realistic fruit stack with a large amount of fruit into a geometrical model is rather challenging. Three dimensional videogrammetry techniques with 3D laser camera setups can extract the global outer shape of the fruit filling pattern with good detail, but, unfortunately, not its interior structure because the structured light beam cannot reach these parts (Gauthier et al., 2017; Herráez et al., 2016). This hurdle can be circumvented by using X-ray computed tomography (CT) or MRI imaging techniques. CT uses X-ray radiation which can penetrate objects with sufficient depth depending on the mass density

and mass absorption coefficient of the fruit (Herremans et al., 2013). This approach already proved its merit in the characterisation of the internal microstructure of food products in a non-destructive way (Herremans et al., 2014, 2013; Wang et al., 2018), as well as a means to obtain 3D shape models of fruit (Rogge et al., 2015, 2014). Since X-rays are mainly attenuated by the fruit and not the air, this technique provides a useful method to visualize and model realistic fruit stacks.

In this study, CT imaging of randomly filled pear fruit in a cardboard package was performed for three different cultivars (cv. ‘Doyenné’, cv. ‘Conference’ and cv. ‘Durondeau’). The images were used to reconstruct a 3D geometrical model, which captures the actual filling pattern inside the package. These geometries were incorporated in a CFD model of a horizontal FAC process and the simulations were validated with experimental data of temperature measurements inside different fruit inside the package during cooling in a FAC setup. The setup consisted of a plenum connected to a fan that draws cooled air into the package from a cooling room.

2 Materials and methods

2.1 Pear fruit

Fruit from three pear cultivars (*Pyrus communis*, cv. ‘Durondeau’, cv. ‘Conference’ and cv. ‘Doyenné’) were collected on September 25th, 2017 from a commercial grower (Van Der Velpen; Bierbeek, Belgium). The pears were picked late August 2017 within the optimal picking window, as determined by the Flanders Centre of Postharvest Technology (VCBT, Belgium). The pears were stored for one month under ambient atmosphere at −0.5 °C. All pears were free of visual defects. The differences between the pear cultivars were characterised by calculating the hydraulic diameter, the elongation factor and the sphericity. For the non-spherical pear fruit, the hydraulic diameter (d_p) is defined as (Gaskell, 2012):

$$d_p = \left(\frac{6V}{\pi} \right)^{\frac{1}{3}} \quad (1)$$

120 with V the pear volume [m^3]. The elongation factor presents the ratio between the width and
 121 the length of the fruit relative to its mass centre. Fruit that are elongated have low values.
 122 The sphericity (Φ) of an individual pear was calculated as the ratio of the surface area of a
 123 sphere with equivalent particle volume to the surface area of the pear (A ; [m^2]; (Wadell,
 124 1935)):

$$\Phi = \frac{\pi^{\frac{1}{3}} (6V)^{\frac{2}{3}}}{A} \quad (2)$$

125 2.2 Fruit box

126 In this study, a telescopic, single layer corrugated fibreboard cardboard (CFC) box
 127 design (LC Packaging, Sint-Katelijne-Waver, Belgium) with outer dimensions of 50 cm \times
 128 33 cm \times 31 cm and a 0.3 cm wall thickness was used to fill fruit into. The short side has one
 129 large horizontally oriented, rectangular vent hole (i.e., the handle) on the top middle region,
 130 resulting in a total open area of 2.45 %. No vent holes were present on the long sides of the
 131 box. One box per cultivar was randomly filled with pears not according to a pattern, resulting
 132 in an average weight of 25.55 kg \pm 0.28 kg per box. The total number of pear fruit was
 133 104, 122 and 114 for ‘Doyenné’, ‘Conference’ and ‘Durondeau’, respectively. Figure 1
 134 shows the dimensions of the box design and the three randomised pear-filling patterns that
 135 were obtained after CT image reconstruction.

136 2.3 CT image reconstruction

137 Cross-sectional slices of the three boxes filled with pears in which thermocouples were
 138 placed in selected ‘sample fruit’, were obtained with X-ray CT imaging on October 3rd, 2017.
 139 The X-ray CT scans were made with a Siemens Somatom (KU Leuven, Gasthuisberg,
 140 Belgium), operating at a tube setting of 140 kV and 500 mA to capture 1900 projection

images. The voxel dimension was $0.9766 \times 0.9766 \times 0.3000$ mm. After obtaining the X-ray CT scans, image analysis was done with Avizo 9.5 (FEI, Bordeaux, France). Due to the distinctive greyscale intensity of the box, all pixels marking the box were easily manually removed from the volume, prior to segmentation of the pears and thermocouple wires. Next, the greyscale data were converted to binary via a histogram based multi-thresholding module with manual corrections (Wang et al., 2018). With the image histogram, the number of pixels with a specific grey value in the image were counted. This histogram was analysed based on multi-phase Otsu thresholding (Otsu, 1979) which separated the histogram statistically into three discrete levels that corresponded to air, fruit and thermocouples. By selecting proper greyscale values, images were segmented in pear objects and thermocouple wiring. Subsequently, all segmented pear objects were separated from each other by subjecting them to watershed segmentation. In this algorithm, the Euclidean distance map (EDM) of the binary image is calculated (Danielsson, 1980; Herremans et al., 2013). The EDM can be interpreted as a topographic map of a terrain with mountain peaks (regions of solid objects) and local valleys (air regions). If this terrain would be flooded with water, the water would run down the mountain peaks and into the local valleys. By marking these local valleys, the mountain peaks can be separated and correspondingly, the solid objects (Esveld et al., 2012). The watershed algorithm works well to separate convex bodies such as pears (Russ, 2005). In a final step, a surface mesh of the individual pears was exported to ANSYS SpaceClaim (ANSYS, Canonsburg, PA, USA) where small artefacts and protrusions on the surface mesh were manually removed to create a smooth assembly of 3D solid pear bodies. Figure 2 illustrates the followed procedure to generate a 3D geometric model of randomly organised pear fruit, based on X-ray CT images.

2.4 Forced-air cooling experiment

All forced-air cooling experiments were conducted on October 3rd and 4th, 2017 at the VCBT. The three fruit boxes were first equilibrated to ambient air conditions to a temperature of about 16.4 °C. Next, the box was placed with the short side facing the FAC system, located inside a coolstore. This is illustrated in Figure 3. The coolstore was equipped with a cooling unit positioned near the opposite wall to the door side with two ventilators of 0.05 kW each in a ‘blow through’ fan coil configuration. The cooling unit generated a continuous airflow exchange rate of 4280 m³ h⁻¹ and had a refrigeration capacity of 5.5 kW. The FAC airflow was regulated to obtain an airflow rate (0.3 - 1.1 L s⁻¹ kg⁻¹) that is within range of what is commonly used in the industry (ASHRAE, 2010; Brosnan and Sun, 2001). The airflow rate was measured at a single point at the end of the circular air shaft with an anemometer (TSI VelociCalc 9545, Kritech & Co PGmbH, Belgium; accuracy of ± 0.015 m s⁻¹). The log-Tchebycheff rule for circular duct airflow measurements was used to correlate the single point measurement and the airflow rate (ASHRAE, 2013). The temperature and relative humidity of the cool stores were kept at -0.46 ± 0.17 °C and $87\% \pm 1\%$, respectively, for all experiments. The FAC system used a centrifugal fan (G2E140AI2801, EBM-Papst, Benelux B.V.) that drew the refrigerated air through the box. The pressure drop over the box was measured with a differential pressure sensor (GEMS Sensors, Hampshire, UK; accuracy of ± 1 Pa). Fruit pulp temperatures of twelve pears at distinct positions in the carton (‘sample fruit’) were monitored every 15 s with T-type thermocouples (OMEGA Engineering, USA; accuracy of ± 0.025 °C). The exact positions of the thermocouples inside the fruit are illustrated in Figure 4.

2.5 Data analysis

2.5.1 Internal pore network characterisation

Due to the random organisation of the pears, the air pore network inside the box was completely different for each pear filling. Based on the binary images of the CT scans, this pore network was characterised by calculating the size distribution of the individual pores and the number of branch points in the network. With a skeletonisation process of the binary images, all the air spaces in the 3D binary volume were reduced to interconnected lines, located in the middle of the air space. Counting the points where multiple lines intersected resulted in the branch number. Next, the Euclidean distance map was calculated by computing the distance between every individual air voxel to the closest pear voxel. This provided the pore size distribution throughout the network based on the voxel size. By combining the result of the skeletonisation process with the Euclidean distance map, the pore network with the actual local pore sizes was reconstructed. Porosity was calculated as the proportion of the voxels of air in the binary image to the total number of voxels.

Another important parameter to characterise the airflow through the pore network is the tortuosity. The geometrical tortuosity is defined as the ratio of the average length of the porous paths in a given direction to the length of the volume of interest in this direction (Pardo-Alonso et al., 2014). Computing the geometric tortuosity from 3D images was performed with Matlab (The MathWorks Inc., Natick, MA) and was based on the TORT3D algorithm developed by Al-Raoush and Madhoun (Al-Raoush and Madhoun, 2017). In brief, the algorithm also started from binary images and conducted a search for connected paths in the flow direction. First, starting points for the connected pores were chosen. Since the local porosity near the walls of the box is high, a smaller volume of interest was taken than the size of the box size used and, thus, sliced the fruit located near the wall region. This ensured that only the internal tortuosity of the pear fillings was calculated. Next, a set of porous paths

213

τ :

$$\tau = \frac{\sum_{i=1}^n l_{p_i}}{l_s} \quad (3)$$

214

where l_p is the length of a single connected pore; l_s the length the volume of interest in the

215

flow direction, and n the number of calculated pores.

216

2.5.2 Temperature heterogeneity between different fruit

217

The fractional unaccomplished temperature difference can be used to describe and

218

analyse the cooling behaviour of each individual horticultural produce (Brosnan and Sun,

219

2001). This parameter is presented in Eq. 4:

$$Y_{t,n} = \frac{T_{t,n} - T_m}{T_{i,n} - T_m} \quad (4)$$

220

where the subscript i represents the initial fruit temperature [K]; m the set cooling medium

221

(i.e., the supply air in the cold store) temperature [K]; t the time step and n the indicator of

222

an individual sample fruit; T indicates the temperature at a certain time t in the core of the

223

sample fruit [K]. Two prevalent cooling characteristics are the half cooling time (HCT;

224

$\bar{Y}_t = 0.500$) and seven-eighths cooling time (SECT; $\bar{Y}_t = 0.125$). The average fractional

225

unaccomplished temperature change (Eq. 4) can be used as a dimensionless time scale to

226

continuously and adequately compare different cooling processes with each other (Olatunji

227

et al., 2017):

$$\bar{Y}_t = \sum_{n=1}^m \frac{Y_{t,n}}{m} \quad (5)$$

228

where m represents the total number of sample fruit used to follow the cooling process.

In general, every cooling process starts at $\bar{Y}_t = 1$ and progresses towards $\bar{Y}_t = 0$. During the cooling process, the majority of the fruit will cool near the average cooling rate. However, fruit located near vent holes or in isolated regions in the box tend to cool faster or slower, respectively (Gruyters et al., 2018). This will create both cold and hot spots in the box, which can be illustrated by the dimensionless temperature difference, ΔY :

$$\Delta Y_{t,n} = Y_{t,n} - \bar{Y}_t \quad (6)$$

Positive values of Eq. 6 represent fruit that are warmer than average (hot spots) while negative values represent fruit that are colder than average (cold spots).

2.6 Numerical modelling procedure

2.6.1 CFD model

Computational models of the three boxes filled with a different pear cultivar were constructed. The physical transport phenomena in the airspaces between the fruit were explicitly resolved. The free-stream air was modelled as a fluid domain while both fruit and box design were modelled as solid domains. The thermophysical model parameters of the box, the fruit and the air were assumed temperature independent due to the relatively small temperature range (Ferrua and Singh, 2009c), and are presented in Table 1.

The initial cooling rate of the FAC process was about 7°C in the first hour, corresponding to more than 150 W. The initial respiration heat generation at 20°C of the pears in a single box would be about 3 to 4 W (ASHRAE, 2010). Thus, the small contribution of respiratory heat to the total heat load is only relevant for prolonged cooling operations (Redding et al., 2016) and consequently, respiration heat generation was not taken into account in the model (Gowda et al., 1997; Tanner et al., 2002). Due to the negligible weight loss during FAC processes (Tanner et al., 2002), the latent heat removal by moisture evaporation at the surface of the fruit was assumed insignificant. This was verified based on a computational analysis of the evaporation rate in the conditions of the cooling experiment,

based on peel permeability and total mass transfer coefficient analysis of pears (Nguyen et al., 2007). In addition, buoyancy effects and radiation were assumed to have a minimal effect in FAC processes (Defraeye et al., 2013a) and were also not taken into account.

Figure 5 presents the computational domain with the implemented boundary conditions (BCs), simulating a horizontal FAC process of a single box. At the inlet of the fluid domain, an ambient atmospheric pressure condition was imposed to resemble the cool store environment. On the fluid flow entering the computational domain, a sufficiently low turbulence intensity of 5 % was imposed as the air in the room was at low velocity and therefore anticipated to have low turbulence fluctuations. At the air domain outlet, a negative pressure was imposed to simulate the operation of the centrifugal fan in the FAC system (see Table 2). By ensuring sufficient difference between the up- and downstream sections, the influence of these boundaries on the fluid flow near the box was minimised. All other sides of the air domain were modelled as a symmetry BC. The box was modelled as no-slip walls with zero roughness with a fixed temperature BC on the outer box walls similar to the cool store temperature (~ -0.35 °C), while the conduction through the box was modelled using properties provided in Table 1. The Reynolds-averaged Navier-Stokes (RANS) equations combined with the shear stress transport $k-\omega$ turbulence model (SST $k-\omega$ model) and wall functions were solved. The SST $k-\omega$ model used automatic wall functions to automatically switch from a low- Re formulation to wall functions (ANSYS, 2014), which were used to predict the heat exchange at the interfaces between the fruit and air (Defraeye et al., 2013b). This turbulence model was validated previously for a very similar computational setup (Ambaw et al., 2013; Defraeye et al., 2013a; Delele et al., 2013b, 2008; Gruyters et al., 2018; Han et al., 2015; Wu et al., 2018). The flow quantities in the boundary-layer region were modelled with a fine grid resolution to ensure low y^+ values. First, steady-state simulations of the airflow and heat transfer of the filling patterns were performed, using

a constant fruit surface temperature of 20 °C and airflow entering the computational domain at 0 °C. These simulations were used to identify distributions of air velocity and pressure losses over the packages. Next, a transient heat transfer simulation similar to the experimental conditions was performed to evaluate the cooling performance via the time-dependent temperature changes calculated at the same location as the thermocouples used in the experiment. The inlet cooling air temperature and initial fruit temperature were taken the same as the average value measured in the experiment (see Table 2).

2.6.2 Solution procedure

A hybrid mesh grid with tetrahedral and hexahedral mesh cells was used to discretise all domains. In total, the ‘Doyenné’, ‘Conference’ and ‘Durondeau’ models had 4.29×10^6 , 4.58×10^6 and 4.28×10^6 mesh cells. A grid sensitivity analysis with Richardson extrapolation was performed to calculate the spatial discretization error (Celik et al., 2008; Franke et al., 2007; Roache, 1994). For the pressure drop over the box and the surface-averaged heat transfer coefficients of the fruit, the spatial discretisation error was maximally 2.9 % for all computational models.

The model transport equations were solved using the finite volume technique of ANSYS CFX 19.0. The iterative procedure was evaluated by monitoring the velocity and temperature at certain locations in the flow field, as well as the mass imbalance and the turbulent kinetic energy. First, the mass and momentum equations were solved after which a converged steady-state solution for the airflow was used as an initial condition to solve the unsteady heat transfer equations. Based on a temporal sensitivity analysis, a time step of 120 s with 35 iterations was selected for the transient simulations. The advection scheme used a high-resolution spatial differencing scheme and the transient scheme the second-order backward Euler method, which is an implicit time-stepping scheme that is second-order accurate (ANSYS, 2016). All calculations were performed on a 64-bit Intel® Xeon® CPU

E5-2630, 2.30 GHz, 128 GB RAM, Windows 7 PC. All transient simulations (for a period of 24 h after cooling) took more than 56 h to complete.

3 Results

3.1 Geometrical features of the three pear cultivar filling patterns

The ‘Conference’ pears in the experiment were significantly smaller in terms of hydraulic diameter, fruit weight and volume than the other two cultivars (Table 3). Although more fruit could be placed inside the box, the total fruit volume in each box was similar ($25.55 \text{ kg} \pm 0.28 \text{ kg}$). In addition, the ‘Conference’ filling pattern was a bit denser compared to the other filling patterns, resulting in a lower overall porosity in the box (Table 3). Both ‘Doyenné’ and ‘Durondeau’ have higher sphericity and elongation values compared to ‘Conference’. This means that the former two cultivars are more spherically shaped compared to the long, oblong-shaped ‘Conference’ cultivar. Because of its elongated shape, the surface-to-volume ratio of ‘Conference’ was considerably higher than for ‘Doyenné’ and ‘Durondeau’. The values of the latter two cultivars (Table 3) were comparable to values reported for apples and spheres in literature (Gruyters et al., 2018).

3.2 Pressure drop characteristics

Both the experimental and numerical pressure drop characteristics over a single box filled with the three pear cultivars and one without pears are presented in Figure 6. The experimental pressure drop data of ‘Doyenné’ showed a similar trend as the virtual empty box, indicating that there was likely excessive leakage during this experiment. Therefore, this data was excluded from the analysis.

A reasonable agreement can be observed between the numerical and experimental pressure drop characteristics. The shape of the curves matches, but slightly higher pressure drop values were measured experimentally compared to the numerical simulation results.

During the experiments, it was observed that there was no perfect alignment of the vent positions on the inner and outer box, which is a common and recurring problem in telescopic CFC boxes. This increases the pressure drop and can explain a mismatch with CFD simulations. With the numerical models, the contribution of the filling pattern to the overall pressure drop was calculated to be maximally 3 % for all three pear filling patterns. The main contribution to the pressure drop is the box (Gruyters et al., 2018) and not the fruit filling pattern as is shown in both experiments and the model results.

3.3 Internal porosity characterisation and airflow patterns

Table 4 presents the branch number of the pore network and the geometrical tortuosity in the flow direction based on Eq. 3. In addition, the maximum pore size that 50 % and 90 % of all pore volumes in the network have, were also presented in Table 4. Although the pore network in the ‘Conference’ filling pattern was more branched, most of the pores in the network were 13 % and 22 % smaller compared to ‘Durondeau’ and ‘Doyenné’, respectively. In addition, its tortuosity was 14.8 % lower than the other filling patterns, implying that the incoming air travels along a more direct path towards the end of the box.

Figure 7a presents a visualisation of all connected paths in the flow direction used to calculate the tortuosity. For ‘Conference’, most of these paths were located either in the top or bottom region of the box. However, it was observed that the connected paths of ‘Doyenné’ and ‘Durondeau’ are rather well distributed throughout the filling pattern. The pore channel network in the right side of the box is illustrated in Figure 7b. A high degree of porosity was present near the box walls, resulting in large, local pore channel sizes. The larger branching of air pores in the ‘Conference’ filling pattern also resulted in numerous small pores in the middle of the box. For the other two filling patterns, relatively large pore channels were visible going from the top towards the bottom of the box. In combination with the higher tortuosity value, these filling patterns had a larger degree of aeration.

Figure 8 displays velocity vectors and a velocity contour plot in a right vertical plane of the pear box. Since the box design had a single vent located in the top region of the box, an air stream was created, blowing at high velocity over the pears situated in the top zone of the box. For the ‘Conference’ filling pattern, the airflow in the middle region of the box seemed to be blocked by the horizontal, interlocking filling arrangement of the pears. Together with the small pore channel sizes in this region (see Figure 7b), a zone that was exposed to significantly lower velocities, compared to the other two filling patterns, was created. In the bottom region near the front side, larger pore channels were present and small air recirculation zones were observed.

3.4 Cooling behaviour of pear fruit

For all three pear filling patterns, time-temperature profiles of the sample fruit were experimentally obtained and compared with the numerical simulation results. Figure 9 presents an example of the cooling profiles obtained from the sample fruit of ‘Doyenné’, located on the right side of the box with a distinction between the top and bottom part of the box. The numerical results agreed well with the experiments. Fruit located in the top part of the box were exposed to high airflow velocities. Consequently, the top fruit cooled significantly faster than the bottom fruit. In addition, a progressive cooling front was observed, going from the front towards the back of the box. Heat withdrawn from the fruit warms the incoming air, resulting in a slower cooling process in the back of the box.

The seventh-eighth cooling time (SECT) of the numerical results had the highest difference of 9 % with the experiments (Table 5). Also the minimum and maximum values of experiments and CFD results correspond well, thus both are providing similar insight into the cooling rate variation across the box. The predicted SECT of the different fruit measured in each box aligns well with the experimental value (Figure 10). The RMSE of the SECT

values were 10.3 min , 16.8 min and 12.5 min for ‘Conference’, ‘Durondeau’ and ‘Doyenné’, respectively; or between 4.3 and 6.5 % of the average predicted SECT value.

There was no significant difference in average cooling rate between the three pear filling patterns. However, a large difference was noted between the minimum and maximum SECT values. For ‘Conference’, this difference was even 33 % higher than for the other two filling patterns, for which the range was of a similar magnitude.

To visualise the spatial temperature distribution inside the three pear boxes, temperature contour plots in the right vertical plane of the pear box after 0.5 h and 1.5 h of cooling are presented (Figure 11). Clearly, large temperature differences exist between the top and bottom region of the box. In addition, most pears located in the front cooled faster than in the back region of each box.

The temperature heterogeneity over time can be visualised by plotting ΔY (Eq.6) of individual sample fruit over time as a function of \bar{Y}_t (Eq. 5) (Figure 12). Both at the start and near the end of the cooling process, the temperature heterogeneity is low as most fruit have similar initial temperatures and have reached the temperature in the cold storage ($\pm 0.49^\circ\text{C}$), respectively. Fruit having ΔY -values around 0 cooled similar to the average cooling rate. The largest temperature variability was observed for the ‘Conference’ filling pattern. Especially around the half cooling time (HCT), the temperature heterogeneity was highest which is a clear indication that the cooling behaviour is cultivar dependent. Further, from Fig. 11 it appears that variation of cooling rates of a cultivar such as ‘Conference’ is even larger than between cultivars.

4 Discussion

The results in this study showed clear effects of fruit shape and filling on heat transfer uniformity in boxes during cooling. The more non-spherical the product, the more non-uniform the cooling behaviour was across the box, both in experiments and in CFD

simulation results. There appears to be a complex interplay between shape and size of the fruit and the pore network of the air spaces, resulting in a more variable cooling rate for ‘Conference’ in comparison to the others. The standard deviation of the SECT (Table 5) is the largest for ‘Conference’, while the fruit sphericity and porosity are smallest, with smallest pore size and highest number of branches. The total porosity of the different boxes was almost equal, and the air space was highly branched in each case. The small pores will provide a higher resistance to airflow thus likely providing less aeration to zones with small air spaces. ‘Durondeau’ and ‘Conference’ had similar pore size distributions, but in the latter filled cartons the smaller pores were more concentrated in the centre bottom of the box. The ‘Durondeau’ and ‘Doyenné’ stacks also had a higher streamwise tortuosity, indicating more mixing across the main airflow direction (see Figure 7). The structural features also explain the slightly higher pressure drop across the ‘Durondeau’ box that was observed in the simulations: this stack has both smaller pores and a higher tortuosity (see Figure 6). Pressure drop, however, played a minor role in this application, where the main pressure loss is caused by the box vent holes, similar to the results of previous works (Delele et al., 2008; Gruyters et al., 2016). This indicates that size and position of vent holes remain the critical parameters in fruit box design.

Aliasing in CT images occur if the voxel resolution of the images is insufficient. In that case, the edges of objects in cross-sectional slices will seem ragged or errated. By performing anti-aliasing, the average greyscale value of neighbouring pixels is calculated to smooth the uneven edges. As can be seen from Figure 2, there was a distinct difference between the air (black) and fruit regions (higher pixel intensity) in the raw X-ray CT image. The next step in the CT image reconstruction is converting the greyscale data to binary images. Via a histogram based multi-thresholding module, the optimum threshold is calculated to separate these two classes so that the inter-class variance is maximal. However, an increase or

decrease in voxels appointed to the fruit would have an effect on the final geometry. The outcome of this procedure will eventually determine the internal pore network of each reconstructed pear filling pattern. To get an idea about the sensitivity of the procedure, a single box filled with known volumes (for example spheres) could be reconstructed. By calculating and comparing the volume of each reconstructed sphere with its realistic shape, an error estimate is obtained. For relevant fruit volumes, a segmentation error of a single pixel (here 1 mm) will result in 2.5 % error in diameter or 8 % in volume. In terms of cooling rates, the cooling time scales with the square of the diameter, which thus results in an error of less than 6%. This complies with the relative RMSE errors found for the SECT.

Although CT-based reconstruction of the actual filling pattern allows a very accurate one-to-one comparison with experiments, it required access to CT equipment to make the X-ray CT scans of individual boxes and image processing knowledge for the subsequent geometry reconstruction. The total image processing time amounted up to 15 working days in order to produce a CAD geometry that is suitable for simulations. Therefore, it does not permit for fast analyses of fruit box cooling operations, while also providing only a particular filling pattern for each measured box. Design and engineering applications generally require an independent research platform that can be used throughout the year without being limited by the seasonal availability of the fruit (Gross et al., 2016). Developing explicit CFD models with the combination of the Discrete Element Method (DEM) and the stochastic shape model generator as discussed by Gruyters et al. (2018) takes biological variability into account without a need for experimental input beyond initial shape model development. With this approach, multiple fruit filling patterns in a specific box design can be generated to account for local differences in the fruit cooling behaviour. Therefore, the DEM-CFD approach is favoured for future package design studies.

5 Conclusions

In this study, a methodology for constructing a geometrical model of the actual filling pattern of fruit inside boxes from CT images was successfully demonstrated. An individual fibreboard box was filled with three different pear cultivars ('Doyenné', 'Conference' and 'Durondeau') after which horizontal forced-air cooling experiments were performed to validate the CFD models. There was a good agreement between experimental and numerical simulation, resulting in a maximum SECT difference of 9 %. The contribution of the filling pattern to the overall pressure drop over the box was low, i.e. 3 %; still, important cooling differences between boxes were observed. Due to the interlocking filling arrangement of 'Conference' pears, vertical airflow was obstructed which resulted in a low velocity region in the bottom of the box. This implies that size and position of vent holes are critical parameters for box design. The airflow obstruction in the middle of the box caused the development of a very large temperature heterogeneity inside the box. Furthermore, the internal porosity characterisation of the 'Doyenné' and 'Durondeau' filling pattern was rather similar to each other but very different from the 'Conference' filling pattern. Clearly, the cooling behaviour is affected by fruit shape in particular filling patterns, and the temperature variability within fruit of the same cultivar may be larger than the variability between cultivars.

The CFD modelling validated in this study is equal to that described by Gruyters et al. (2018) and thus validates their DEM-CFD approach. The latter technique avoids the need of X-ray CT scans and image processing while relying on statistical shape models of fruit. This will allow to incorporate variability in filling patterns in the analysis in a comprehensive modelling effort for package and cooling process design purposes.

Acknowledgements

This work was supported by Flanders Innovation & Entrepreneurship (projects VLAIO 120745 and VLAIO HBC.2016.0395).

References

- Al-Raoush, R.I., Madhoun, I.T., 2017. TORT3D: A MATLAB code to compute geometric tortuosity from 3D images of unconsolidated porous media. *Powder Technol.* 320, 99–107. <https://doi.org/10.1016/j.powtec.2017.06.066>
- Ambaw, A., Mukama, M., Opara, U.L., 2017. Analysis of the effects of package design on the rate and uniformity of cooling of stacked pomegranates: Numerical and experimental studies. *Comput. Electron. Agric.* 136, 13–24. <https://doi.org/10.1016/j.compag.2017.02.015>
- Ambaw, A., Verboven, P., Delele, M.A., Defraeye, T., Tijskens, E., Schenk, A., Nicolai, B.M., 2013. CFD Modelling of the 3D Spatial and Temporal Distribution of 1-methylcyclopropene in a Fruit Storage Container. *Food Bioprocess Technol.* 6. <https://doi.org/10.1007/s11947-012-0913-7>
- ANSYS, 2016. ANSYS CFX 17.2 Reference Guide. ANSYS, Inc., Canonsburg, PA, USA.
- ANSYS, 2014. ANSYS Fluent User's Guide 15.0.
- ASHRAE, 2013. ASHRAE: Handbook - Fundamentals.
- ASHRAE, 2010. ASHRAE Handbook: Refrigeration. Atlanta.
- Berry, T., Fadji, T.S., Defraeye, T., Opara, U.L., 2017. The role of horticultural carton vent hole design on cooling efficiency and compression strength: A multi-parameter approach. *Postharvest Biol. Technol.* 124, 62–74. <https://doi.org/10.1016/j.postharvbio.2016.10.005>
- Brosnan, T., Sun, D.W., 2001. Precooling techniques and applications for horticultural products - a review. *Int. J. Refrig.* 24, 154–170.
- Celik, I.B., Ghia, U., Roache, P.J., Freitas, C.J., 2008. Procedure for estimation and reporting of uncertainty due to discretization in CFD applications. *J. Fluids Eng.* 130, 4. <https://doi.org/10.1115/1.2960953>
- Danielsson, P.E., 1980. Euclidean distance mapping. *Comput. Graph. Image Process.* 14, 227–248.

500 [https://doi.org/10.1016/0146-664X\(80\)90054-4](https://doi.org/10.1016/0146-664X(80)90054-4)

501 Defraeye, T., Lambrecht, R., Delele, M.A., Tsige, A.A., Opara, U.L., Cronjé, P., Verboven, P.,
502 Nicolai, B., 2014. Forced-convective cooling of citrus fruit: Cooling conditions and energy
503 consumption in relation to package design. *J. Food Eng.* 121, 118–127.
504 <https://doi.org/10.1016/j.jfoodeng.2013.08.021>

505 Defraeye, T., Lambrecht, R., Tsige, A.A., Delele, M.A., Opara, U.L., Cronjé, P., Verboven, P.,
506 Nicolai, B., 2013a. Forced-convective cooling of citrus fruit: Package design. *J. Food Eng.*
507 118, 8–18. <https://doi.org/10.1016/j.jfoodeng.2013.03.026>

508 Defraeye, T., Verboven, P., Nicolai, B., 2013b. CFD modelling of flow and scalar exchange of
509 spherical food products: Turbulence and boundary-layer modelling. *J. Food Eng.* 114.
510 <https://doi.org/10.1016/j.jfoodeng.2012.09.003>

511 Delele, M.A., Ngcobo, M.E.K., Getahun, S.T., Chen, L., Mellmann, J., Opara, U.L., 2013a.
512 Studying airflow and heat transfer characteristics of a horticultural produce packaging system
513 using a 3-D CFD model. Part I: Model development and validation. *Postharvest Biol.*
514 *Technol.* 86, 536–545. <https://doi.org/10.1016/j.postharvbio.2013.08.014>

515 Delele, M.A., Ngcobo, M.E.K., Getahun, S.T., Chen, L., Mellmann, J., Opara, U.L., 2013b.
516 Studying airflow and heat transfer characteristics of a horticultural produce packaging system
517 using a 3-D CFD model. Part II: Effect of package design. *Postharvest Biol. Technol.* 86,
518 546–555. <https://doi.org/10.1016/j.postharvbio.2013.08.015>

519 Delele, M.A., Tijskens, E., Atalay, Y.T., Ho, Q.T., Ramon, H., Nicolaï, B.M., Verboven, P., 2008.
520 Combined discrete element and CFD modelling of airflow through random stacking of
521 horticultural products in vented boxes. *J. Food Eng.* 89, 33–41.
522 <https://doi.org/10.1016/j.jfoodeng.2008.03.026>

523 Diels, E., Smeets, B., Odenthal, T., Keresztes, J., Vanmaercke, S., Verboven, P., Nicolaï, B., Saeys,
524 W., Ramon, H., 2016. Development of a visco-elastoplastic contact force model for arbitrary
525 rounded bodies and determining its contact parameters for apples. *Postharvest Biol. Technol.*
526 120, 157–166. <https://doi.org/10.1017/CBO9781107415324.004>

527 Esveld, D.C., Van Der Sman, R.G.M., Van Dalen, G., Van Duynhoven, J.P.M., Meinders, M.B.J.,

528 2012. Effect of morphology on water sorption in cellular solid foods. Part I: pore scale
 529 network model. *J. Food Eng.* 109, 301–310. <https://doi.org/10.1016/j.jfoodeng.2011.08.016>
 530 Ferrua, M.J., Singh, R.P., 2009a. Modeling the forced-air cooling process of fresh strawberry
 531 packages, Part III: Experimental validation of the energy model. *Int. J. Refrig.* 32, 359–368.
 532 <https://doi.org/10.1016/j.ijrefrig.2008.04.011>
 533 Ferrua, M.J., Singh, R.P., 2009b. Modeling the forced-air cooling process of fresh strawberry
 534 packages, Part II: Experimental validation of the flow model. *Int. J. Refrig.* 32, 349–358.
 535 <https://doi.org/10.1016/j.ijrefrig.2008.04.009>
 536 Ferrua, M.J., Singh, R.P., 2009c. Modeling the forced-air cooling process of fresh strawberry
 537 packages, Part I: Numerical model. *Int. J. Refrig.* 32, 335–348.
 538 <https://doi.org/10.1016/j.ijrefrig.2008.04.010>
 539 Franke, J., Hellsten, A., Schlünzen, H., Carissimo, B., 2007. Best practice guidelines for the CFD
 540 simulation of flows in the urban environment. COST Action 732 Qual. Assur. Improv.
 541 microscale Meteorol. Model. Hamburg, Ger.
 542 Gaskell, D.R., 2012. An introduction to transport phenomena in materials engineering, 2nd ed.
 543 Momentum Press, LLC, New York, USA. <https://doi.org/10.5643/9781606503577>
 544 Gauthier, S., Puech, W., Bénéière, R., Subsol, G., 2017. Analysis of digitized 3D mesh curvature
 545 histograms for reverse engineering. *Comput. Ind.* 92–93, 67–83.
 546 <https://doi.org/10.1016/j.compind.2017.06.008>
 547 Gowda, B.S., Narasimham, G.S.V.L., Murthy, M.V.K., 1997. Forced-air precooling of spherical
 548 foods in bulk: A parametric study. *Int. J. Heat Fluid Flow* 18, 613–624.
 549 [https://doi.org/10.1016/S0142-727X\(97\)00028-3](https://doi.org/10.1016/S0142-727X(97)00028-3)
 550 Gross, K.C., Wang, C.Y., Saltveit, M., 2016. The commercial storage of fruits, vegetables, and
 551 florist and nursery stocks, 5th Editio. ed. USDA, Agricultural Research Service.
 552 <https://doi.org/10.1007/978-1-4613-1127-0>
 553 Gruyters, W., Rogge, S., Vanmaercke, S., Delele, M., Ramon, H., Verboven, P., Nicolai, B., 2016.
 554 DEM-CFD of cooling of packed fruit using 3D shape models, in: CIGR AgEng Conference,
 555 26-29 June 2016. Aarhus, Denmark, p. 4p.

Gruyters, W., Verboven, P., Diels, E., Rogge, S., Smeets, B., Ramon, H., Defraeye, T., Nicolai, B.M., 2018. Modelling Cooling of Packaged Fruit Using 3D Shape Models. *Food Bioprocess Technol.* 11, 2008–2020. <https://doi.org/10.1007/s11947-018-2163-9>

Han, J.W., Qian, J.P., Zhao, C.J., Yang, X.T., Fan, B.L., 2017. Mathematical modelling of cooling efficiency of ventilated packaging: Integral performance evaluation. *Int. J. Heat Mass Transf.* 111, 386–397. <https://doi.org/10.1016/j.ijheatmasstransfer.2017.04.015>

Han, J.W., Zhao, C.J., Yang, X.T., Qian, J.P., Fan, B.L., 2015. Computational modeling of airflow and heat transfer in a vented box during cooling: Optimal package design. *Appl. Therm. Eng.* 91, 883–893. <https://doi.org/10.1016/j.applthermaleng.2015.08.060>

Herráez, J., Martínez, J.C., Coll, E., Martín, M.T., Rodríguez, J., 2016. 3D modeling by means of videogrammetry and laser scanners for reverse engineering. *Meas. J. Int. Meas. Confed.* 87, 216–227. <https://doi.org/10.1016/j.measurement.2016.03.005>

Herremans, E., Bongaers, E., Estrade, P., Gondek, E., Hertog, M., Jakubczyk, E., Nguyen Do Trong, N., Rizzolo, A., Saeys, W., Spinelli, L., Torricelli, A., Vanoli, M., Verboven, P., Nicolai, B., 2013. Microstructure-texture relationships of aerated sugar gels: Novel measurement techniques for analysis and control. *Innov. Food Sci. Emerg. Technol.* 18. <https://doi.org/10.1016/j.ifset.2013.02.003>

Herremans, E., Verboven, P., Defraeye, T., Rogge, S., Ho, Q.T., Hertog, M.L.A.T.M., Verlinden, B.E., Bongaers, E., Wevers, M., Nicolai, B.M., 2014. X-ray CT for quantitative food microstructure engineering: The apple case. *Nucl. Instruments Methods Phys. Res. Sect. B Beam Interact. with Mater. Atoms* 324. <https://doi.org/10.1016/j.nimb.2013.07.035>

Jackson, J.E., 2003. The biology of apples and pears - Biology of horticultural crops. Cambridge University Press, Cambridge, United Kingdom.

Kader, A.A., 2002. Postharvest technology of horticultural crop, 3rd ed. UCANR Publications, Richmond.

Lu, L., Chen, X., Wang, J., 2016. Modelling and thermal analysis of tray-layered fruits inside ventilated packages during forced-air precooling. *Packag. Technol. Sci.* 29, 105–119. <https://doi.org/10.1002/pts.2189>

584 Nguyen, T.A., Verboven, P., Schenk, A., Nicolaï, B.M., 2007. Prediction of water loss from pears
 585 (*Pyrus communis* cv. Conference) during controlled atmosphere storage as affected by
 586 relative humidity. *J. Food Eng.* 83. <https://doi.org/10.1016/j.jfoodeng.2007.02.015>
 587 Olatunji, J.R., Love, R.J., Shim, Y.M., Ferrua, M.J., East, A.R., 2017. Quantifying and visualising
 588 variation in batch operations: A new heterogeneity index. *J. Food Eng.* 196, 81–93.
 589 <https://doi.org/10.1016/j.jfoodeng.2016.10.004>
 590 Otsu, N., 1979. A threshold selection method from gray-level histograms. *IEEE Trans. Syst. Man.*
 591 *Cybern.* 9, 62–66. <https://doi.org/10.1109/TSMC.1979.4310076>
 592 Pardo-Alonso, S., Vicente, J., Solórzano, E., Rodriguez-Perez, M.A., Lehmhus, D., 2014.
 593 Geometrical Tortuosity 3D Calculations in Infiltrated Aluminium Cellular Materials. *Procedia*
 594 *Mater. Sci.* 4, 145–150. <https://doi.org/10.1016/j.mspro.2014.07.553>
 595 Prusky, D., 2011. Reduction of the incidence of postharvest quality losses, and future prospects.
 596 *Food Secur.* 3, 463–474. <https://doi.org/10.1007/s12571-011-0147-y>
 597 Redding, G.P., Yang, A., Shim, Y.M., Olatunji, J., East, A., 2016. A review of the use and design
 598 of produce simulators for horticultural forced-air cooling studies. *J. Food Eng.* 190, 80–93.
 599 <https://doi.org/10.1016/j.jfoodeng.2016.06.014>
 600 Roache, P.J., 1994. Perspective: a method for uniform reporting of grid refinement studies. *J.*
 601 *Fluids Eng.* 116, 405–413.
 602 Rogge, S., Beyene, S.D., Herremans, E., Hertog, M.L., Defraeye, T., Verboven, P., Nicolai, B.M.,
 603 2014. A Geometrical Model Generator for Quasi-Axisymmetric Biological Products. *Food*
 604 *Bioprocess Technol.* 7. <https://doi.org/10.1007/s11947-013-1169-6>
 605 Rogge, S., Defraeye, T., Herremans, E., Verboven, P., Nicolaï, B.M., 2015. A 3D contour based
 606 geometrical model generator for complex-shaped horticultural products. *J. Food Eng.* 157.
 607 <https://doi.org/10.1016/j.jfoodeng.2015.02.006>
 608 Russ, J.C., 2005. Image analysis of food microstructure. CRC Press. [https://doi.org/10.1016/B978-](https://doi.org/10.1016/B978-0-12-373904-9.50001-5)
 609 [0-12-373904-9.50001-5](https://doi.org/10.1016/B978-0-12-373904-9.50001-5)
 610 Smeets, B., Odenthal, T., Keresztes, J., Vanmaercke, S., Van Liedekerke, P., Tijssens, E., Saeys,
 611 W., Van Oosterwyck, H., Ramon, H., 2014. Modeling contact interactions between

triangulated rounded bodies for the discrete element method. *Comput. Methods Appl. Mech. Eng.* 277, 219–238. <https://doi.org/10.1016/j.cma.2014.04.017>

Taiz, L., Zeiger, E., Møller, I.M., Murphy, A., 2015. *Plant physiology and development*, 6th ed. Sinauer Associates, Inc., Sunderland, Massachusetts U.S.A.

Tanner, D.J., Cleland, A.C., Opara, U.L., Robertson, T.R., 2002. A generalised mathematical modelling methodology for design of horticultural food packages exposed to refrigerated conditions: part 1, formulation. *Int. J. Refrig.* 25, 33–42. [https://doi.org/10.1016/S0140-7007\(01\)00019-6](https://doi.org/10.1016/S0140-7007(01)00019-6)

Wadell, H., 1935. Volume, shape, and roundness of quartz particles. *J. Geol.* 43, 250–280.

Wang, Z., Herremans, E., Janssen, S., Cantre, D., Verboven, P., Nicolai, B., 2018. Visualizing 3D Food Microstructure Using Tomographic Methods: Advantages and Disadvantages. *Annu. Rev. Food Sci. Technol.* 9, 323–343. <https://doi.org/10.1146/annurev-food-030117-012639>

Wu, W., Cronjé, P., Nicolai, B., Verboven, P., Linus Opara, U., Defraeye, T., 2018. Virtual cold chain method to model the postharvest temperature history and quality evolution of fresh fruit – A case study for citrus fruit packed in a single carton. *Comput. Electron. Agric.* 144. <https://doi.org/10.1016/j.compag.2017.11.034>

Zhao, C.J., Han, J.W., Yang, X.T., Qian, J.P., Fan, B.L., 2016. A review of computational fluid dynamics for forced-air cooling process. *Appl. Energy* 168, 314–331. <https://doi.org/10.1016/j.apenergy.2016.01.101>

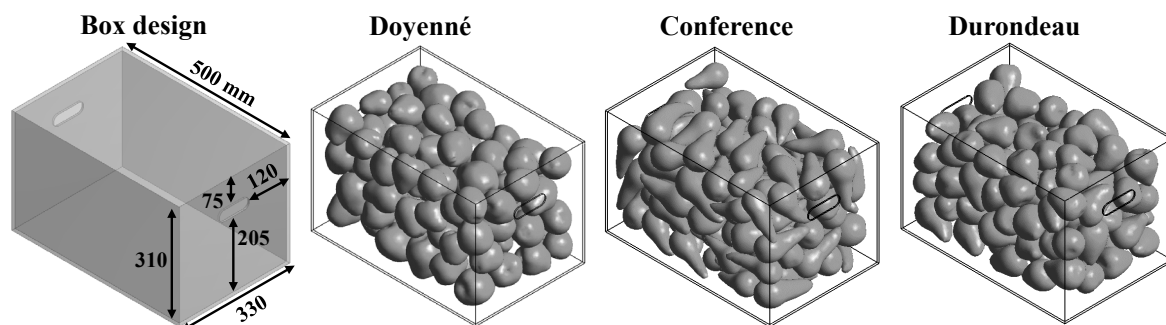


Figure 1: Geometrical representation of the box design and corresponding stack fillings based on CT images of packaged fruit of three pear cultivars.

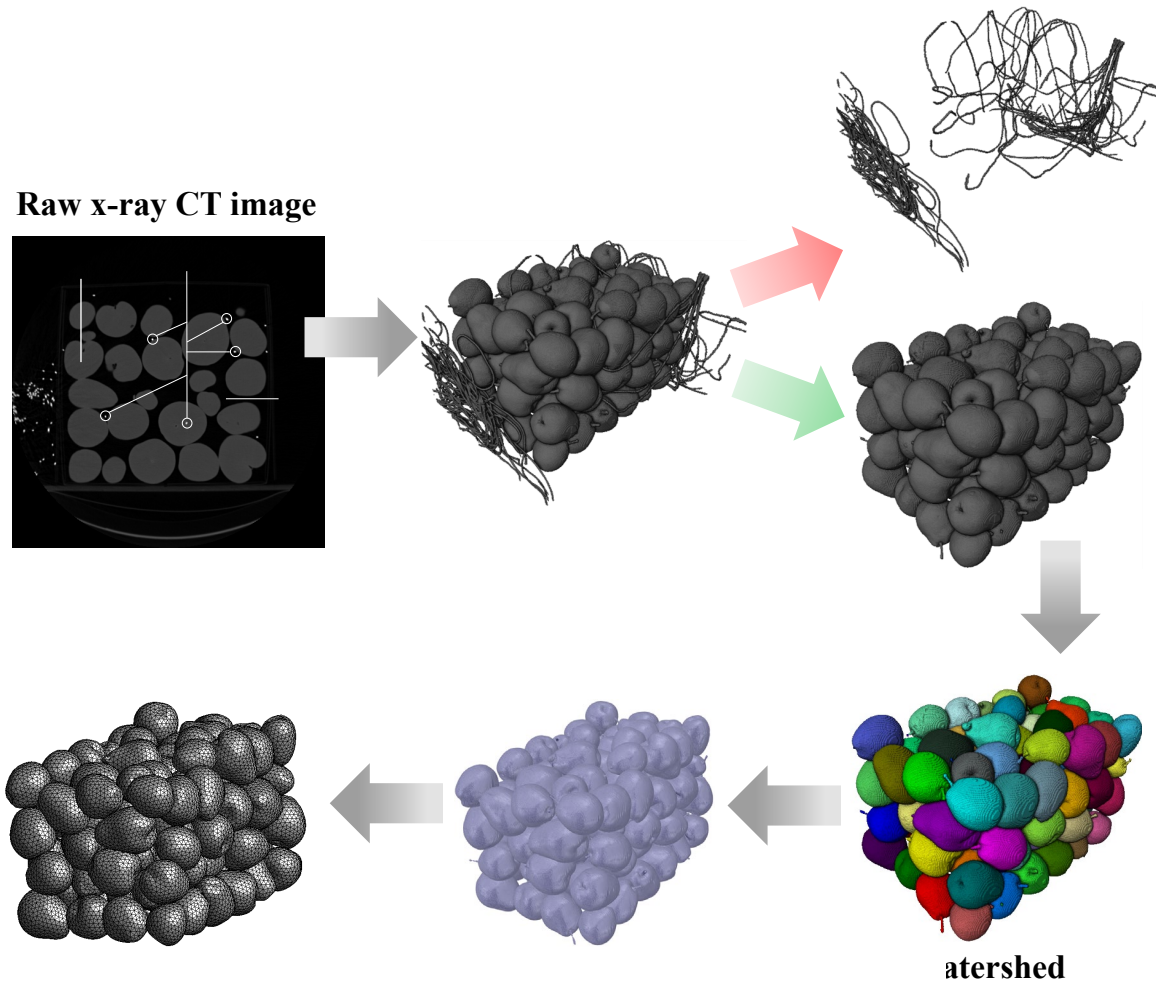


Figure 2: General overview of the methodology used to reconstruct a smooth assembly of 3D solid pear bodies from raw X-ray computed tomography images.

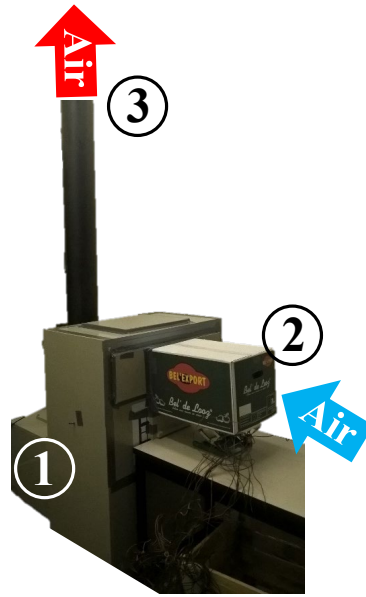
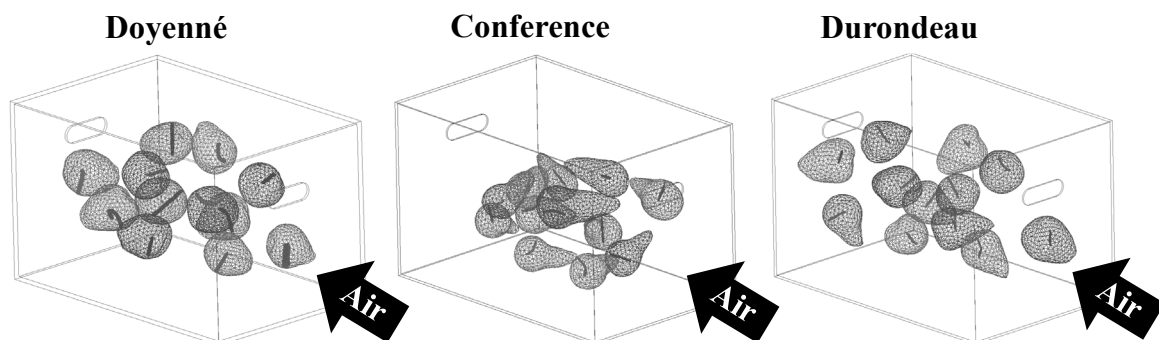


Figure 3: The experimental forced-air cooling setup with 1) the location of the centrifugal fan; 2) the box filled with pear fruit and thermocouples; 3) position of anemometer to measure the airflow rate. The cold air is drawn into the setup via the right-hand side (indicated with the blue arrow) and leaves the setup via the long, vertical air shaft (indicated with the red arrow).

653
654



656
657
658
659
660

Figure 4: The relative position of the 12 sample fruit in the filling and the corresponding location of the thermocouples inside the fruit for the three pear cultivars. In all three boxes, six fruit were located both in the top and bottom region and were evenly distributed on each side along the depth direction to distinguish a front, middle and back region in the box.

661

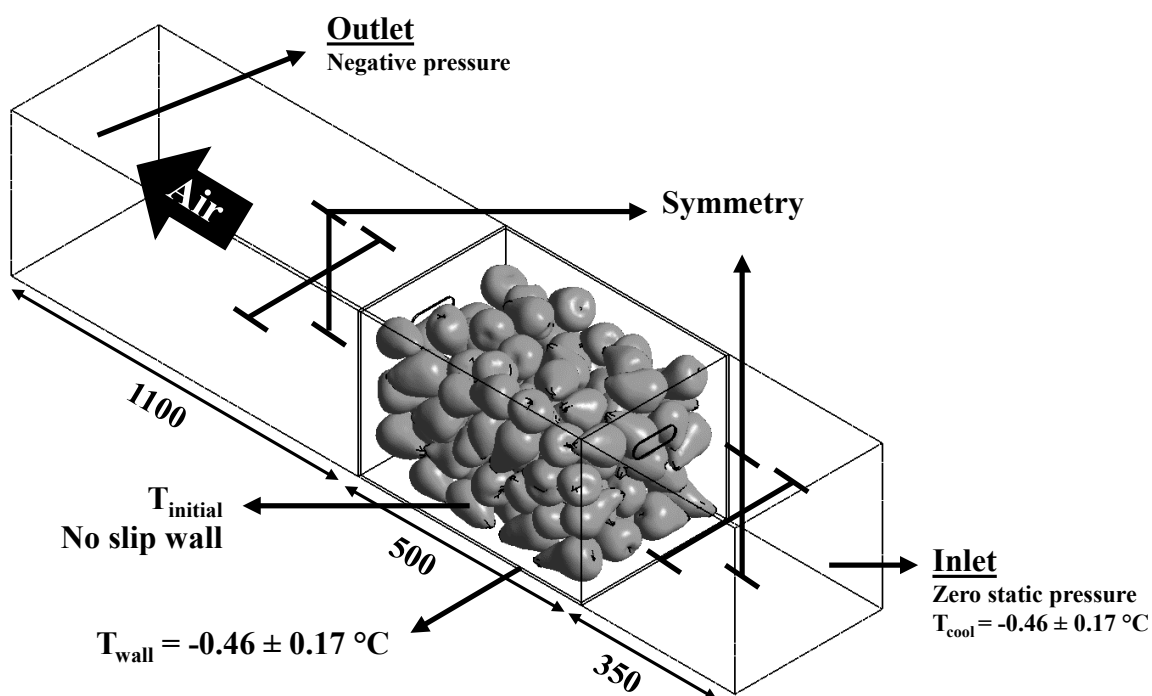


Figure 5: Schematic overview of the CFD model. The implemented boundary conditions were the same for all pear geometries. The air enters the computational domain from the right-hand side. The dimensions are expressed in mm.

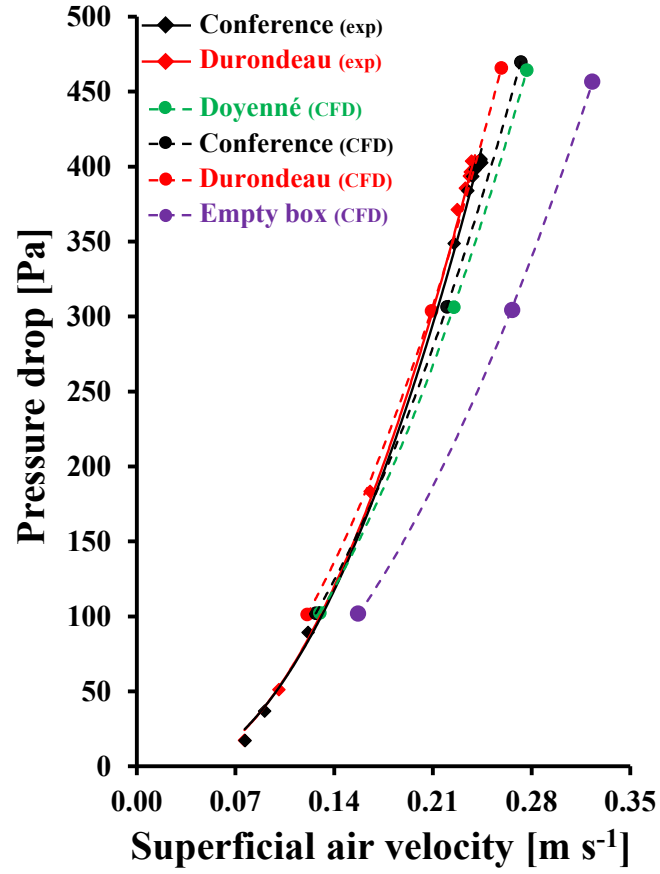


Figure 6: Pressure drop [Pa] over a single box filled with three different pear cultivars as a function of superficial air velocity [m s⁻¹]. The experimental data points of the Conference and Durondeau filling patterns (diamonds) and the numerically obtained values for an empty box and three pear filled boxes (spheres) with their polynomial approximation are displayed.

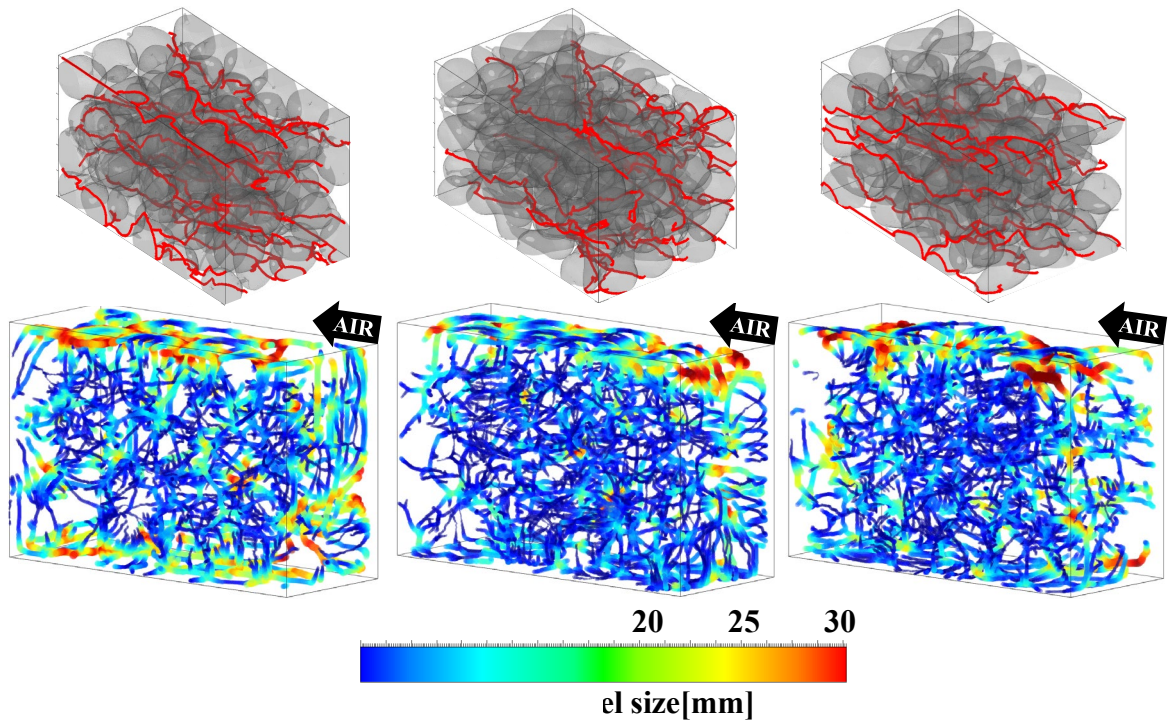


Figure 7: a) Visualisation of all connected paths through the box in the flow direction of the three pear filling patterns; these connected paths were used to calculate the geometrical tortuosity described by Eq. 3; b) visualisation of the internal pore network in the right box region.

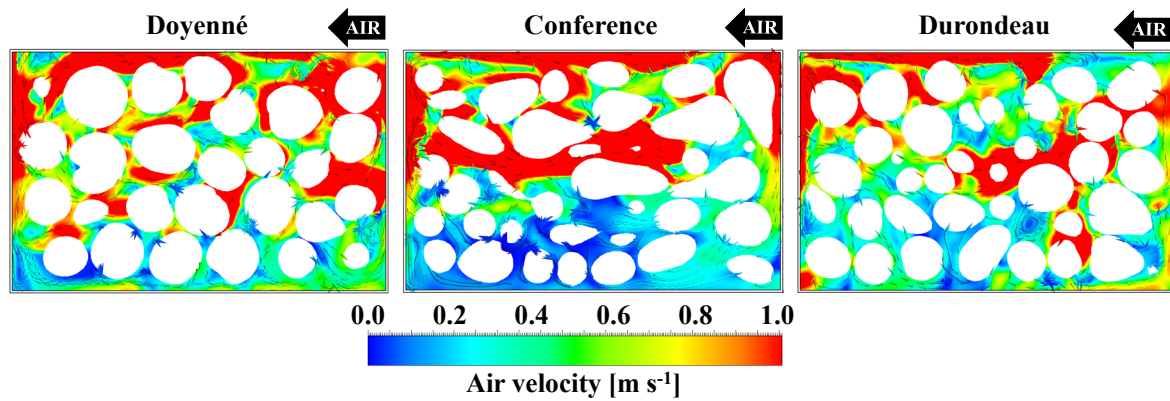
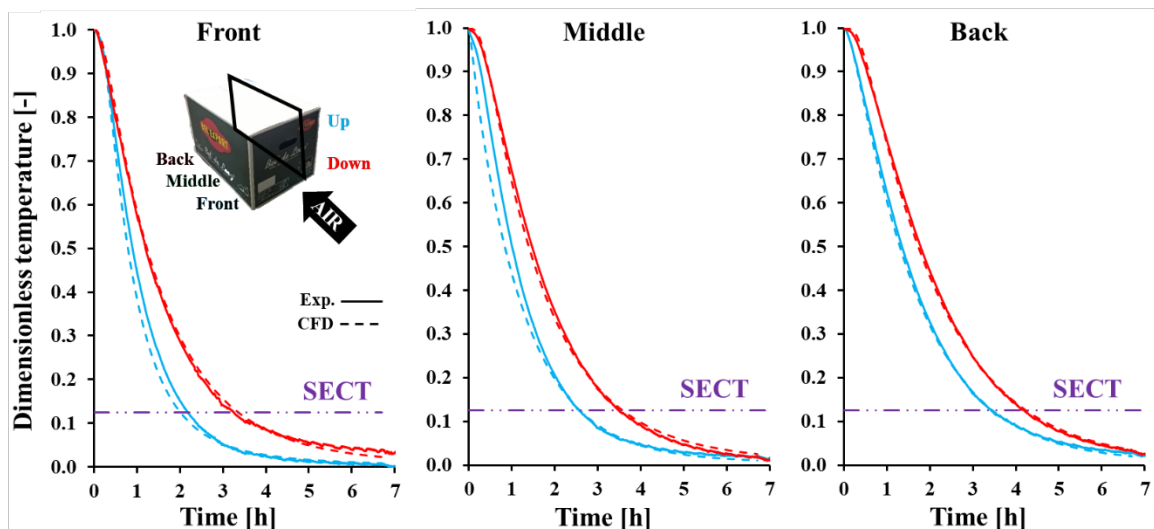


Figure 8: Velocity contour plots and velocity vectors for the experimental flow rate conditions (Table 2) in the right vertical plain of the pear boxes. The air enters the computational domain from the right-hand side.

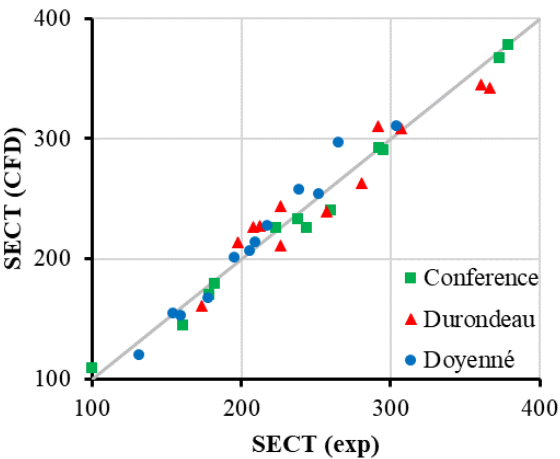
688
689



691 **Figure 9: An example of the experimentally measured and corresponding numerically calculated**
692 **temperature profiles of the sample fruit located on the right-hand side in the single box filled with Doyenné pears.**
693 **A distinction was made between the pear fruit located in the front (left), middle (centre), back (right) region and**
694 **between the top (blue line) and bottom (red line) region of the box.**

695

696



698

699

700

701

Figure 10: Correspondence of seventh-eight cooling time (SECT) between experiments and CFD for the three boxes filled with different cultivars of pear.

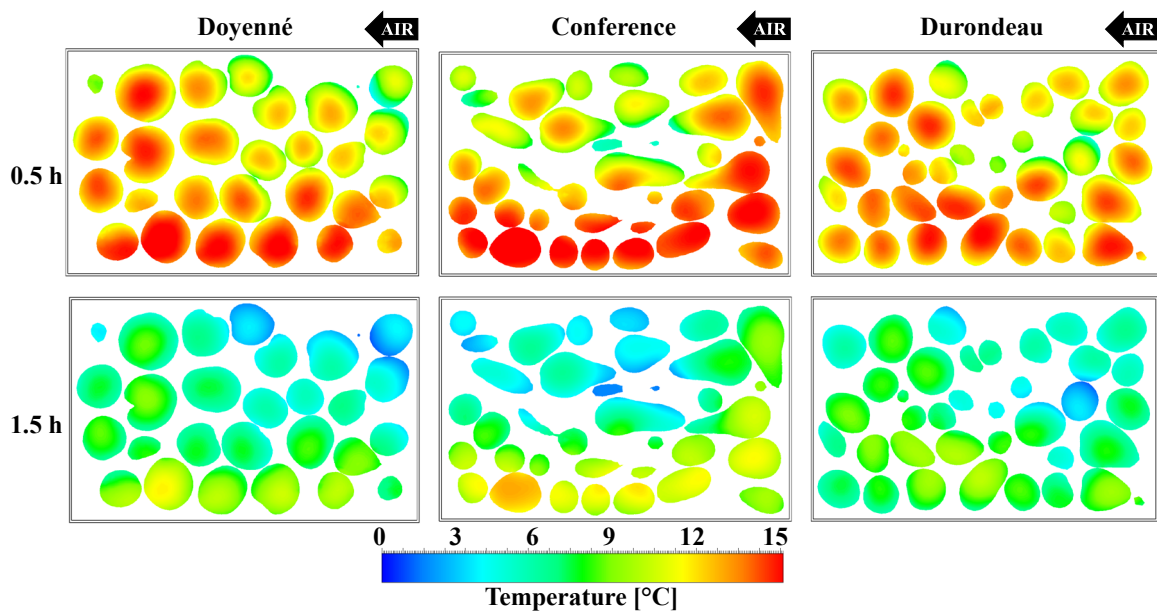


Figure 11: Temperature contour plots in the right vertical plain of the pear boxes after 0.5 h and 1.5 h of cooling. The air enters the computational domain from the right-hand side.

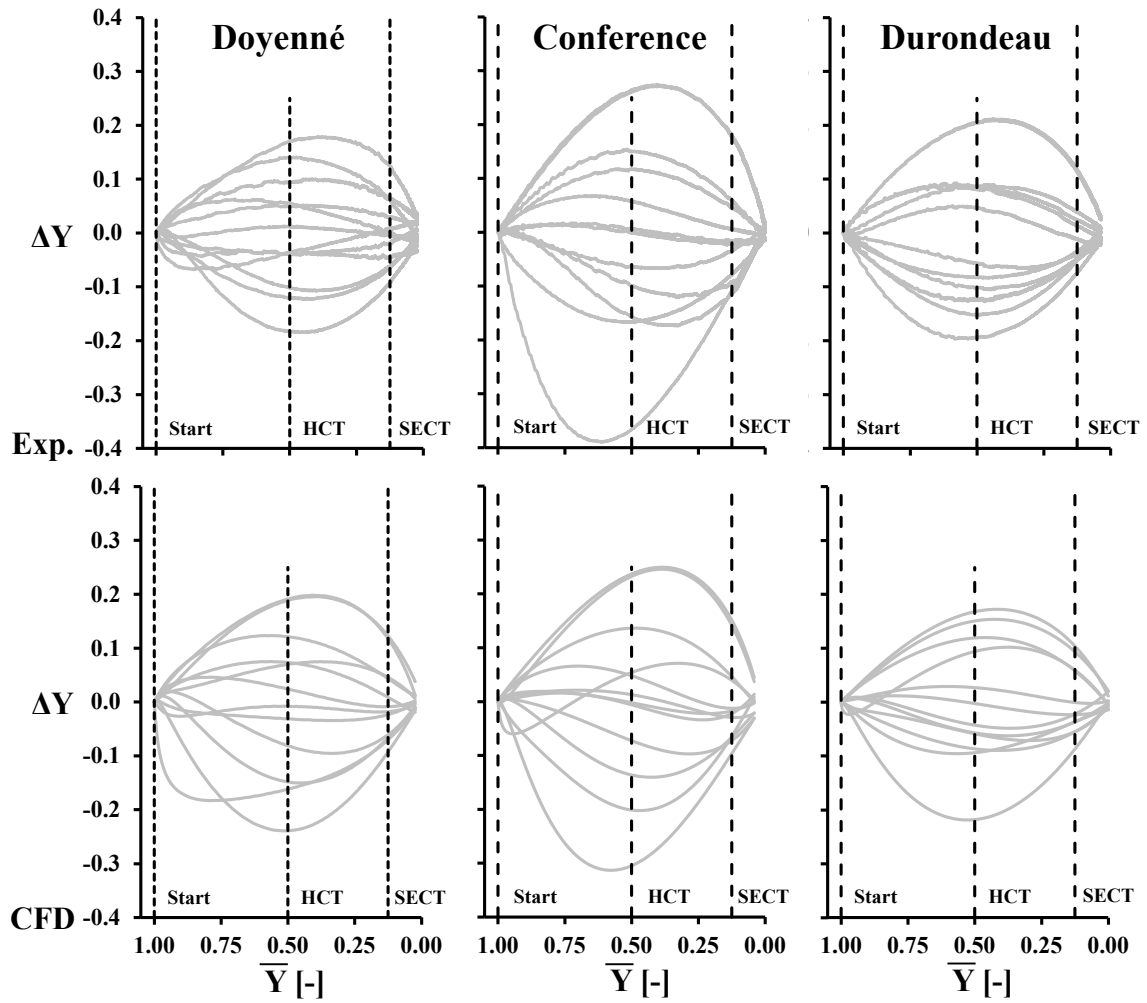


Figure 12: Temperature heterogeneity plots for the forced-air cooling of the three different pear filling patterns, plotting ΔY of individual fruit against the average Y value of the sample fruit (\bar{Y}) for both the experimental (top row figures) and numerical results (bottom row figures).